

attenuation, L_{rain} [dB] (see Figure A.4), and the temperature of the rain droplets, estimated as $290K$. The system temperature increase is then:

$$T_{rain} = \left(1 - 10^{-\frac{L_{rain}}{10}}\right) T_{droplets} \tag{A.11}$$

Given the system-noise temperature and the temperature increase due to the rain, it is possible to calculate the sensitivity of the receiving station, G_r/T_s [dB]:

$$G_r/T_s = G_r - 10 \log_{10} (T_s + T_{rain}) \tag{A.12}$$

The performance of the entire communication link is expressed by the signal-to-noise ratio that can now be computed with Eq. (A.13), where all the parameters are in dB. This value will then be compared to the required one to compute the link-margin.

$$E_b/N_0 = EIRP - L_{pr} - L_{pt} - L_s - L_a + G_r + 10 \log_{10} (k) - 10 \log_{10} (T_s + T_{rain}) - 10 \log_{10} (R) \tag{A.13}$$

In equation (A.13), k is the Boltzmann constant, $k = 5.67051 \text{ W/m}^2\text{K}^2$, and R is the link data-rate in *bps*. Subtracting between 1 and 2 dB for implementation losses from the E_b/N_0 , the margin between the required (see Figure A.1) and the calculated signal-to-noise ratio can be estimated. The link margin should be larger than the rain attenuation value, with some safety margins (3 to 4 dB).

A.1.2 Mass and power estimation

To estimate the mass of the antenna(e), we work with data collected from Wertz and Larson (1999b). From these data, it is possible to derive a relationship that links the aperture area of the antenna to its mass. We can estimate an average density of $12 - 13 \text{ kg/m}^2$. Therefore, an estimation for the mass of the antenna can be obtained multiplying the aperture area by the average density. For what concerns the transmitter mass and power estimation, a similar approach has been pursued. In Figure A.5, we show a graph that presents the trends of transmitters mass and power as a function of the power output. A distinction has to be made on the type of transmitters. TWTA is the acronym of Traveling Wave Tube Amplifier; it is the classical amplifier tube, usually used for analog communications. Solid-state amplifiers have been developed in the recent years. Those are amplifiers based on printed circuits, capable of giving the same performance in terms of power output, that the TWTA provides with much less mass, much less volume and higher power consumption. The *type of transmitter* is also an example of a categorical variable.

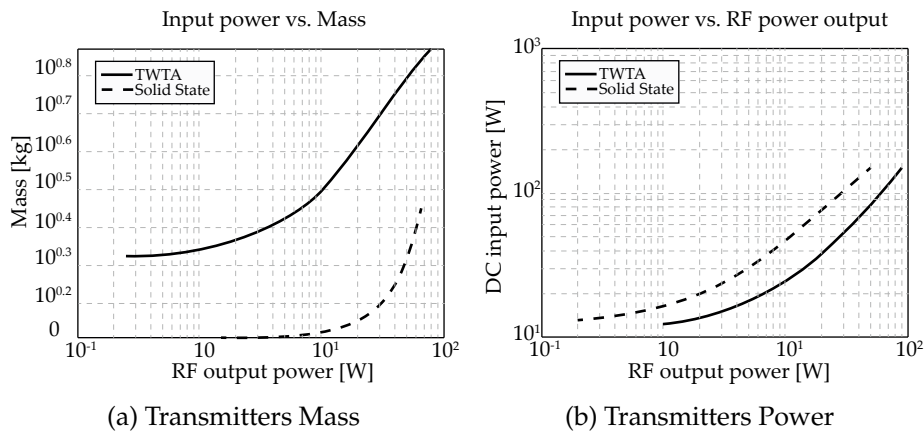


Figure A.5 Satellite transmitter mass and power vs. RF power output. Figure adapted from Wertz and Larson (1999b).

A.2 Power subsystem

The amount of power that the satellite's subsystems require is one of the driving inputs for the design of the power subsystem. The duration of the mission is an important input as well. It strongly affects the process of selection and design of the power sources and energy storage hardware. The longer the mission lasts the more performance is required from this subsystem. The hardware degrades with time in the space environment (Solar Particle Events, Galactic Cosmic Rays, etc.); the power sources must be designed for the End-Of-Life (EOL) conditions with the required power as input, which in a conservative assumption may be assumed equal to the power required at the Beginning-Of-Life (BOL). This usually results in an overdesign of the subsystem for the BOL conditions.

The satellite's orbit influences the power subsystem design in terms of solar radiation conditions. It must be clear that the main source of energy in space, especially for Earth-oriented missions, is the energy coming from the Sun. As function of the orbital parameters of the orbit, the satellite may encounter eclipse periods, where the Earth hides the radiation coming from the Sun. In those periods, the power subsystem must provide the power required anyway therefore the energy storage hardware must be properly designed. The eclipse conditions drive the selection and the design of the energy storage hardware.

Another important aspect related to the orbit of the satellite is the amount of energy coming from the Sun. It varies with the inverse square of the distance from the Sun itself. Considering only Earth-oriented missions an average value of 1367 W/m^2 for the solar radiation constant is usually taken into account. For power sources that use the energy coming from the Sun, the angle with which the Sun light impinges on the spacecraft affects the design of the power sources themselves. Usually, for those typologies of power sources, the power is proportional to the light direction component perpendicular to the surface. The larger the angle, the lesser the power produced.

A.2.1 Power sources

The power sources that may be used for space missions are several, *e.g.*, photovoltaic, chemical thermal, solar thermal, nuclear thermal, RTGs, primary batteries, and fuel cells. Some of these power sources have already been flown in missions performed in the past, while some others are under development or under the process of being adapted for space missions. The power sources taken into account in the model and presented in this section, are photovoltaic, solar thermal, nuclear and radioisotope based power sources. The *type of power source* is an example of categorical variable used in the design of the power subsystem.

Solar arrays

The first step in the design of a solar array for a spacecraft is the selection of the typology of solar cells to use with their efficiency and power density characteristics. For space applications two types of solar cells, namely crystal silicon, *c-Si*, and Gallium-Arsenide, *GaAs*, are most widely used. Other parameters that determine the performance of the solar array are the power losses along the path from the array to the batteries or the loads. The time in which the spacecraft is in eclipse and the power required by the spacecrafts subsystems, consent to calculate the required power from the solar arrays, P_{sa} [W]:

$$P_{sa} = \frac{\frac{P_e T_e}{X_e} + \frac{P_d T_d}{X_d}}{T_d} \quad (\text{A.14})$$

The parameters P_e and P_d , expressed in W, represent the power requirements during eclipse and during sun illumination. They may be taken equal in a conservative way. The parameters T_e and T_s , expressed in s, represent the time in which the satellite is in eclipse or in sun light, during the orbit. The parameters X_e and X_d , expressed in s represent the power losses during eclipse and sun light conditions. The amount of power computed with Eq. A.14 takes into account the power to provide to the loads during light conditions and the power needed to charge the energy storage hardware, in order to be at maximum capabilities for the successive eclipse period. Considering the efficiency of the cell, the amount of energy coming from the Sun that is converted in electrical energy by the solar array is P_0 [W/m^2]:

$$P_0 = 1367\eta_{cell} \quad (\text{A.15})$$

Other losses may occur when the array is built bonding several cells together. Those losses are considered in the inherent degradation, I_d , parameter. The inherent degradation of the solar arrays and the worse case condition angle, θ , with which the sun impinge on the solar arrays consent to calculate the power per unit area at BOL, P_{BOL} [W/m²]:

$$P_{BOL} = P_0 I_d \cos(\theta) \quad (\text{A.16})$$

Considering the yearly degradation of the solar array, and the mission duration, the lifetime degradation of the solar array itself, L_d [%], can be estimated as follows:

$$L_d = (1 - \eta_{degr/year})^{lifetime} \quad (\text{A.17})$$

The power at EOL, P_{EOL} [W/m²], can be calculated from the power @ BOL and the degradation estimated along the lifetime:

$$P_{EOL} = P_{BOL} L_d \quad (\text{A.18})$$

The area of the solar arrays, A_{sa} [m²], required to provide this amount of power per unit area at EOL can be calculated from the total power required:

$$A_{sa} = \frac{P_{sa}}{P_{EOL}} \quad (\text{A.19})$$

The mass of the solar array, M_{sa} [kg], can be calculated from the power required and the power density, ρ_{power} [W/kg], typical for each cell typology, usually around 125 W/kg:

$$M_{sa} = \frac{P_{sa}}{\rho_{power}} \quad (\text{A.20})$$

Primary batteries

An important characteristic of primary batteries is that they cannot be recharged. For this motivation they have been usually implemented in space missions to supply short bursts of power or applications that require a continuative demand of a small amount of power, *e.g.*, computer memory. This is also the motivation why usually this type of battery is considered among power sources rather than energy storage hardware. There are several types of primary batteries. The Silver-Zinc ($Ag - Zn$), were used in space missions like Sputnik, Ranger 3, Mariner 2, etc., Zinc - Mercury oxide ($Zn - HgO$) and Lithium - Sulphur Dioxide ($Li - SO_2$) batteries represent a good alternative to the ($Ag - Zn$) batteries. They were used in space missions like Explorer 1, Galileo probe, and also the Mars Exploration Rover (MER). All these batteries are characterized by having a high specific energy density, approximatively around 120 Wh/kg. From the required power, P_{req} [W], and the operating time (*e.g.*, the duration of the mission), T [h], given the energy density, ρ_{bat} , the mass of the battery can be estimated with the following equation:

$$M_{bat} = P_{req} \frac{T}{\rho_{bat}} \quad (\text{A.21})$$

RTGs

The Radioisotope Thermoelectric Generators, RTGs, are nuclear power sources. Electricity is obtained from the heat generated by the radioactive decay of the fuel, a radioactive isotope, thanks to the Seebeck effect through the utilization of arrays of thermocouples. RTGs have been used in space applications, especially for probes, *e.g.* Cassini-Huygens, New Horizons, Galileo, and Ulysses. The advantage of using RTGs is related to the low power-density, W/kg, that they provide coupled with the fact that the power output is almost constant for a long period of time (depending on the half-time of the isotope used as fuel). The value for the power-density of an RTG, considering also the structure supporting it, can be estimated to be around 10 W/kg. The mass of the RTG can therefore be estimated as follows:

$$M_{RTG} = \frac{P_{req}}{\rho_{RTG}} \quad (\text{A.22})$$

A.2.2 Energy storage

When the selected energy source is *solar arrays*, then the energy must be stored in such a way to have power availability also during the eclipses. The *energy storage* function for space systems is accomplished by the secondary batteries, because they can be recharged, usually thousands of times. The main parameters to be considered are the capacity of the batteries, C [Ah], and their mass, M_{bat} [kg]. The capacity of a battery depends on the power, P_e , required by the spacecrafts subsystems during eclipse periods, the eclipse duration, T_e , the number of batteries N , the voltage of the bus, V [V], the power losses along the path from the batteries to the loads, n [%], and the depth of discharge, DOD [%]. This last parameter indicates how much of the total energy available in a battery is used during one cycle of discharge (one eclipse period).

$$C = \frac{P_e T_e}{DOD \cdot N \cdot n \cdot V} \quad (\text{A.23})$$

Usually the DOD is taken proportional to the number of charge-discharge cycles that the battery encounter in its life. The number of cycles is roughly equal to the number of orbits that the spacecraft perform along its life. The proportionality is inverse, the more the cycles the less should the DOD be. This has been visualized in Figure A.6.

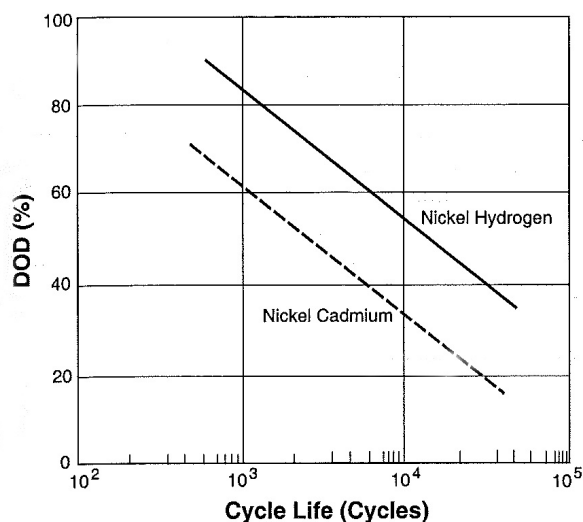


Figure A.6 Depth-of-discharge vs. Cycle Life. Figure adapted from Wertz and Larson (1999b).

The mass of the batteries can be calculated on the basis of the energy density, typical for each typology of battery.

$$M_{bat} = \frac{C \cdot V}{\rho_{energy}} \quad (\text{A.24})$$

The type of batteries used in past space missions, therefore space qualified are Nickel-Cadmium and Nickel-hydrogen. Their energy density is 25-30 [Wh/kg] and 35-57 [Wh/kg], respectively. Further, Lithium-ion and Sodium-Sulfur type of batteries are not space qualified yet, and their energy density is 70-110 [Wh/kg] and 140-210 [Wh/kg], respectively.

A.2.3 Power distribution and regulation

The power produced by the solar arrays must be regulated to the desired voltage, transmitted, controlled and monitored. Heritage from aircraft design implies the voltage to be equal to 28 V DC. Nowadays the tendency is to increase this value to have less power losses. The mass and the power of the equipment of the power distribution and regulation systems are taken proportional to the mass and the power of the spacecraft. The equipment we refer to are the power conditioning unit(s) (PCU), the regulator(s) and converter(s), and the wiring. The mass, in kg, of the PCU, can be estimated as:

$$M_{PCU} = 0.02P_{required} \tag{A.25}$$

The mass and the power of the regulators and converters is estimated as:

$$M_{reg} = 0.025P_{required} \tag{A.26}$$

$$P_{reg} = 0.2P_{required} \tag{A.27}$$

The mass and power of the wiring is estimated as:

$$M_w = 0.03M_{sat-dry} \tag{A.28}$$

$$P_w = 0.02P_{required} \tag{A.29}$$

A.3 Design settings

The design-variable settings used to perform the analysis of the communication and power subsystems, and to obtain the results presented in Chapter 3, are described in the Tables A.2 to A.5.

In Table A.2, we introduce the design variables used for the analysis and their ranges of variation in the design space. There are two continuous variables and three discrete ones. The purpose of this example is not to provide an exhaustive analysis of the coupled communication/power subsystems of a satellite, but to provide an easy-to-grasp logic path to understand the main working principles of the proposed methodologies. Indeed the discrete variables are there to demonstrate the possibility of working with data bases in a structured way. Therefore we considered sufficient to take two or three levels for each of them into account. In this case this means that two or three *items* only have been selected for the analysis from each data base.

In Figure A.7 we show a schematic, an N^2 chart, with the interactions between the communication and power subsystems. Besides links with the subsystem experts and with other subsystems and disciplines, there is one point of attention that is the loop created between the required power (from the communication subsystem) and the available power (from the power subsystem). This type of loops makes the design process iterative and correlates the performance of the two subsystems.

The settings of the discrete variables are described in more detail in Table A.3. Antenna type, the transmitter type, and the parameters related to the solar arrays affect the performances of the two subsystems as discussed in the previous sections.

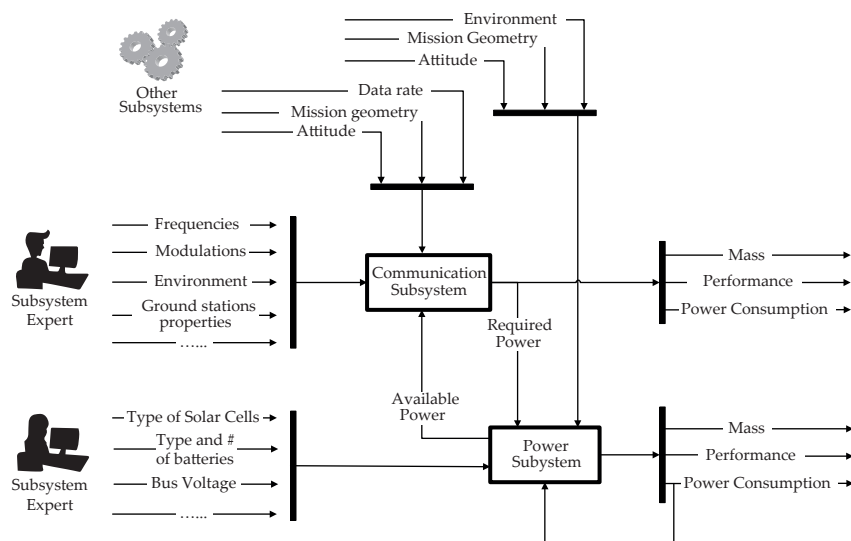


Figure A.7 Schematic representation of the interactions between the communication and power subsystems' models with the subsystem experts and other subsystems and disciplines.

Design Variables	Code	Intervals		Levels
		Min	Max	
Output RF power [W]	A	1	50	–
Antenna diameter [m]	B	0.05	1	–
Type of Antenna [-]	C	1	2	2
Type of Solar Array [-]	D	1	3	3
Type of Transmitter [-]	E	1	2	2

Table A.2 Settings of the design variables.

Type of Antenna	Levels		
	Horn	Aperture	
Type of Solar Array	Silicon	GaAs	Triple Junction
	$\eta_{cell} = 0.148$	$\eta_{cell} = 0.24$	$\eta_{cell} = 0.20$
	$I_d = 0.77$	$I_d = 0.77$	$I_d = 0.60$
	$\eta_{degr/year} = 0.037$	$\eta_{degr/year} = 0.038$	$\eta_{degr/year} = 0.02$
	$\rho_{power} = 115W/kg$	$\rho_{power} = 140W/kg$	$\rho_{power} = 100W/kg$
Type of Transmitter	TWTA	SSPA	

Table A.3 Communication and Power subsystem, discrete design variables settings. Data from Wertz and Larson (1999b).

The analysis of the communication and power subsystems cannot be performed considering them as separate from the other subsystems of the satellite and irrespectively of the orbit that the satellite will undergo. Some boundary conditions need to be set. In Table A.4, the settings of all the parameters that significantly influence the performances of the communication and power subsystems are presented.

		Value
Mission and Orbit	Orbit type	[-] <i>circular</i>
	Orbit Altitude	[km] 1000
	Minimum elevation angle	[deg] 30
	Mission duration	[years] 7
Attitude Control	Antenna pointing offset	[deg] 2
	Sun Incidence Angle	[deg] 23
Payload	Average power consumption	[W] 160
Communication Subsystem	Implementation losses	[dB] 2
	Ground antenna efficiency	[-] 0.55
	Ground antenna pointing offset	[deg] 0.3
	Down-link frequency	[GHz] 2.2
	Down-link data rate	[Mbps] 100
Power Subsystem	Transmission Efficiency (Sunlight)	[%] 71
	Transmission Efficiency (Eclipse)	[%] 62
	Solar Flux	[W/m ²] 1367
	Batteries DoD	[%] 50
	Batteries Energy Density	[W-h/kg] 50

Table A.4 Communication system, settings of other factors influencing the performance.

In Table A.5 we present the settings of the variables for the robust design process that is described in Section 3.4.4. In Section 3.4.4 of this thesis, we present a tentative baseline for the settings of the design variables presented in Table A.2, of which we want to study the robustness to the uncertainties proposed in Table A.5. All the epistemic distributions, and the relative BPA structure, are used when there is no clear information in the literature regarding the uncertainty described. Therefore, factors *I*, *J*, and *D* have been assigned with epistemic uncertainty. Uniform PDF is used for factor *A* and factor *B*. They are controllable design variables, and this uncertainty is related to modification of their value in

subsequent phases of the design process. Normal and log-normal PDFs are used, instead, when there is knowledge of the typical uncertainty distribution of the phenomenon of interest.

Uncertain Variables	Code	Intervals		Distribution	
		Min	Max		
Output RF power	[W]	A	35	45	Uniform
Antenna diameter	[m]	B	0.75	0.85	Uniform
Satellite pointing error	[deg]	C	1	4	Normal ^d
Implementation loss	[dB]	D	1	4	Epistemic ^a
Satellite antenna efficiency	[-]	E	0.45	0.55	Normal ^d
Antenna mass density	[kg/m ²]	F	9	11.5	Log-Normal ^e
Ground antenna efficiency	[-]	G	0.45	0.55	Normal ^d
Ground antenna pointing error	[deg]	H	0.1	1	Log-Normal ^e
Transmission efficiency - Sunlight	[-]	I	0.6	0.8	Epistemic ^b
Transmission efficiency - Eclipse	[-]	J	0.6	0.8	Epistemic ^c
Solar cells η	[%]	K	Nominal ^f - 10%	Nominal ^f + 10%	Log-Normal ^e
Solar array power dens.	[W/kg]	L	Nominal ^f - 10%	Nominal ^f + 10%	Log-Normal ^e
Batteries energy dens.	[W-h/kg]	M	25	75	Log-Normal ^e
Circular orbit altitude	[km]	N	990	1100	Normal ^d
Type of Antenna	[-]		1	2	2 levels
Type of Solar Array	[-]		1	3	3 levels
Type of Transmitter	[-]		1	2	2 levels

Table A.5 Settings of the design variables. ^aIntervals [1, 1.75, 2.5, 3.25, 4], BPA [0.4, 0.25, 0.2, 0.15]. ^bIntervals [0.6, 0.667, 0.773, 0.8], BPA [0.25, 0.4, 0.35]. ^cIntervals [0.6, 0.667, 0.773, 0.8], BPA [0.25, 0.4, 0.35]. ^d $\mu = 0$ $\sigma = 1$, Min and Max are the 0.01 and 0.99 percentile respectively. ^e $\sigma = 1$, Max is the 0.99 percentile, Min corresponds to $X = 0$. ^f See nominal values in Table A.3.

Satellite System for Earth Observation

Earth-observation satellites can observe areas over a wide range rather quickly. It is expected that their observation data combined with information obtained by aircraft and helicopters will be useful for a regular disaster condition assessment. This would make rescue operations more effective, would allow for extracting topographical information reflecting latest land-usage changes, and identifying disaster risks.

In this thesis we use the mathematical model of a satellite to prove and test some of the concepts related to sensitivity analysis and optimization. The mathematical model of the satellite is fractionated into the mathematical models of its subsystems, i.e., payload, Attitude Determination and Control System ADCS, communication, power and avionic, propulsion, structure and thermal control, and cost. The models for communication and power subsystems are these described in detail in Appendix A. The main relationships between the design parameters have been derived from the subsystems' mathematical models available in Wertz (2001); Wertz and Larson (2005, 1999b). As shown in Ridolfi *et al.* (2009, 2010) the implementation of these models has been verified and validated.

The system model is assembled in such a way that once the orbit has been determined and the mission characteristic velocity computed, the payload capability of the launcher for the selected orbit can be determined from Figure B.1, for a given launcher. The launcher characteristic velocity shown there is defined as the total velocity that can be delivered for a given payload after a due east launch from Cape Canaveral and the use of a 185-km parking orbit. We assume that the mission and launcher characteristic velocities are equivalent. In reality, this is only true if the launcher has sufficient coast-restart capabilities, such that this total velocity can be applied to the satellite in the same sequence of increments that were assumed when computing the mission characteristic velocity, Cornelisse *et al.* (1979). The data flow between launcher, satellite, ground segment, and mission models is shown in Figure B.2.

This N^2 chart shows the connections between subsystems in a similar fashion to Figure A.7, in Appendix A. In this case, however, the complexity of the interactions is much higher, having up to three levels of nested loops (*i.e.*, at subsystem level, system level, and inter-disciplinary level between system and mission). For practical reasons only the general overview is shown in Figure B.2.

The cost of the mission is computed summing up the launch cost, and the cost of the satellite system and operations. The Cost Estimating Relationships (CERs) have been derived from Wertz and Larson (1999b, 2005). A hybrid cost model considering the Unmanned Spacecraft Cost Model, USCM, and the Small Satellites Cost Model, SSCM has been implemented. Most of the CERs are related to the mass of the subsystems, the Technology Readiness Level (TRL) the power consumption and the particular technology in use (e.g., three-axis attitude-control technology has a larger cost coefficient than spinned attitude-control technology).

The system model has been used for developing two different Earth-observation applications. These two applications differ in types of objectives and constraints taken into account for two main reasons. One of the applications is developed to test the design methods of Chapter 3, where local methods are implemented, while the other one is developed to show the working principle of the Pareto-robustness concept explained in Chapter 4.

The first application is introduced in Section B.1. It is developed to drive the mission towards having a complete coverage of the Earth surface. The settings and the results for this applicative case are discussed by the author also in ?. The second application, described in Section B.2, is meant to

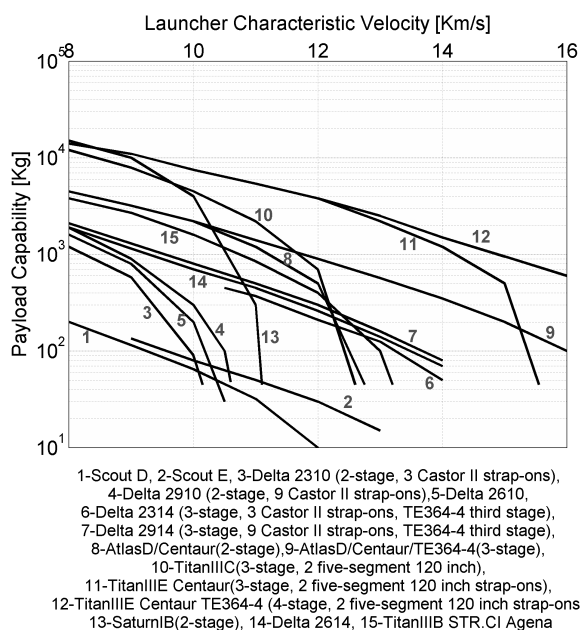


Figure B.1 Launcher payload capability on orbit vs. Launcher characteristic Velocity. Data retrieved from Cornelisse *et al.* (1979) and Wertz and Larson (1999b).

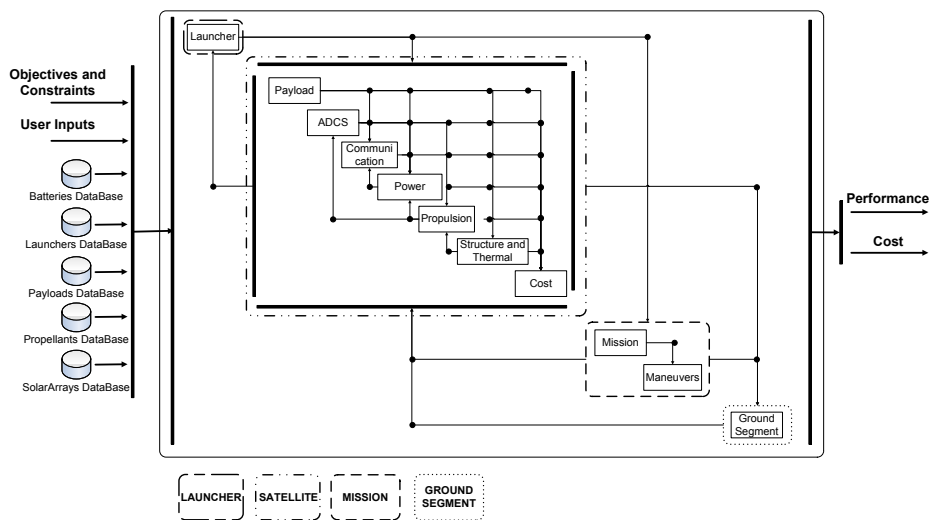


Figure B.2 Schematic of the satellite system with mission segment, launcher and ground segment.

obtain the coverage on a very specific area of the Earth surface, namely the Bay of Bengal. The settings and the results for this applicative case, instead, are discussed by the author also in ?.

B.1 World-wide disaster management

In this section, we describe the mission statement and the main assumptions related to the preliminary design of an Earth-observation mission to support the world-wide disaster management process and land-usage monitoring. The following mission statement is considered as driver for the design process:

Design an Earth observation mission to provide world-wide disaster-management capabilities, over a period of 7 years

The satellite system with an optical payload (staring sensor) is considered. The main purpose is to achieve a compromise between the design variables in such a way to obtain the best possible image

resolution, at minimum cost. The satellite shall revisit the same area on the Earth surface within 24 hours, and shall be able to send the acquired data back, in real time, to any equipped ground station (the reference ground station is considered with 1 m aperture antenna diameter) with a link margin of at least 4 dB. The selected launcher is of the class of the *Delta II 6920/25*, with a maximum payload on polar orbit of 2950 kg. A highly inclined, circular orbit has been selected, with $i = 98^\circ$. The main mission geometry parameters and few of the equations implemented for computing the coverage and the resolution are presented in Figure B.3.

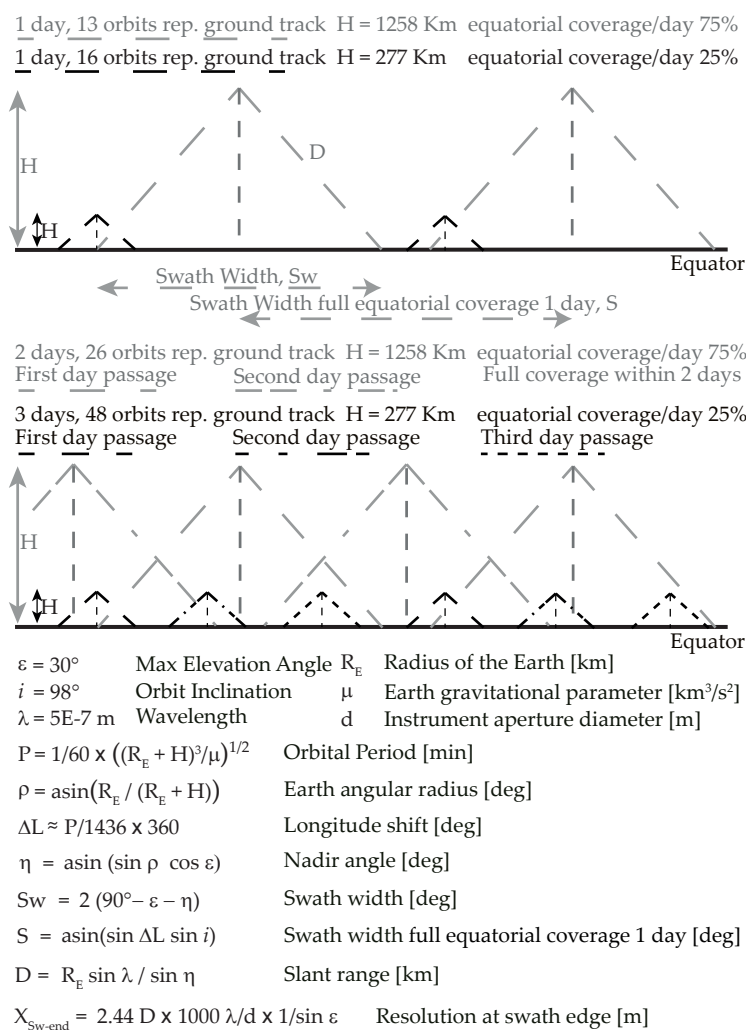


Figure B.3 Satellite mission geometry. Repeating ground tracks and optical-instrument resolution. Equations adapted from (Wertz and Larson, 1999b).

In Table B.1 the design variables taken into account in the analysis, their type and intervals or levels (in case of discrete variables) are summarized.

In Table B.2 the settings for the uncertainty analysis are described.

Two types of solar arrays and two types of thrusters are taken into account. The two types of solar arrays are the Type-1 and Type-3 presented in Table B.5. The two thrusters are the *STAR48A* and the *IUS-SRM2* with a specific impulse of 250 [s] and 300 [s], (Wertz and Larson, 1999b), and a percentage of inert mass with respect to the propellant of 0.13 and 0.21, respectively. The two levels of TRL foresee an *adapted* design from an existing one and a *new* design, respectively. The *new* design is more expensive, but allows for a better management of the acquired data on board, i.e., reduced data rate. The results of the analysis are discussed in Chapter 3.

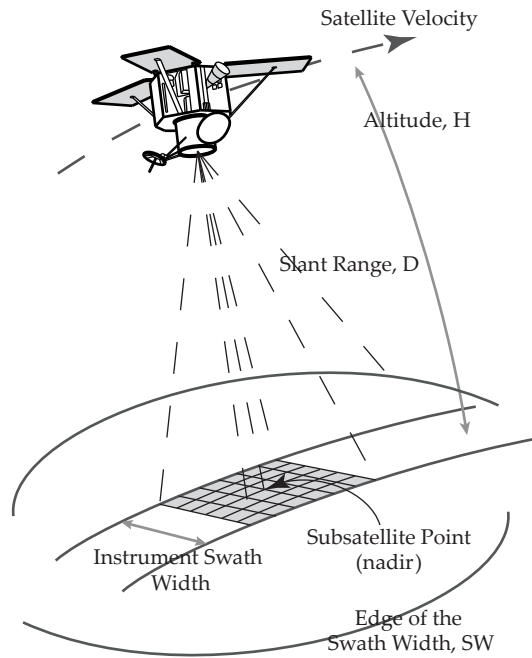


Figure B.4 Satellite ground track representation and geometry on the Earth surface.

Design Variables	Code	Intervals		Levels
		Min	Max	
Number of days (rep. ground track)	A	1	3	3
Number of orbits (rep. ground track) ^a	B	1	3	3
Instrument aperture diameter	C	0.3	1	—
Min. ϵ	D	5	50	—
Max. slewing angle	E	0	50	—
Min. maneuver time	F	60	180	—
Number of slew maneuvers	G	10k	30k	—
Transmitting output RF power	H	5	30	—
Antenna diameter	I	0.1	1	—
Type of solar array	J	1	2	2
Type of thrusters	K	1	2	2
Payload heritage	L	1	2	2

Table B.1 Settings of the design variables.^a When $A = 1$, $B = 13, 14$ or 15 , when $A = 2$, $B = 28, 29$ or 30 , when $A = 3$, $B = 43, 44$ or 45 .

Uncertain Variables		Intervals		Distribution
		Min	Max	
Margin δV	[%]	0	0.25	Epistemic ^a
Specific Impulse	[s]	280	320	Normal ^d
Thrusters inert mass fraction	[%]	0.2	0.4	Epistemic ^b
ADCS sens. mass	[kg]	58	70	Log-normal ^e
ADCS sens. power	[W]	33	45	Log-normal ^e
Antenna mass density	[kg/m ²]	9	11.5	Normal ^d
Solar cells η	[%]	0.17	0.23	Normal ^d
Solar array power dens.	[W/kg]	90	110	Normal ^d
Batteries energy dens.	[W-h/kg]	25	75	Normal ^d
PCU mass	[kg]	27	50	Log-normal ^e
Regulators mass	[kg]	33	55	Log-normal ^e
Thermal subs. mass	[kg]	20	50	Log-normal ^e
Struct. mass margin	[%]	0	1	Epistemic ^c

Table B.2 Settings of the design variables.^aIntervals [0, 0.04, 0.1, 0.17, 0.25], BPA [0.4, 0.3, 0.2, 0.1].
^bIntervals [0.2, 0.25, 0.3, 0.4], BPA [0.4, 0.35, 0.25]. ^cIntervals [0, 0.25, 0.5, 0.75, 1], BPA [0.4, 0.3, 0.2, 0.1].^d $\mu = 0$ $\sigma = 1$, Min and Max are the 0.01 and 0.99 percentile respectively.^e $\sigma = 1$, Max is the 0.99 percentile, Min corresponds to $X = 0$.

B.2 Tsunami emergency management in the Middle-East

On December 26th, 2004, the earthquake of Sumatra-Andaman, the largest seismic event in forty years, produced a devastating tsunami that affected the region of the Indian Ocean called Bay of Bengal and the Indonesian region, Thorne (2005). The regions of Sri Lanka, India, Thailand, Indonesia, Malaysia, and Myanmar particularly suffered the effect of the anomalous waves. The earthquake that caused the tsunami originated at the boundary between the Indo-Australian plate and the southeastern portion of the Eurasian plate. This is an area with particularly high seismic risk, Thorne (2005). Such earthquakes could happen again. To illustrate the working principle of PROA we consider an Earth-observation mission with the following mission statement as driver for the design:

Design an Earth-observation mission to provide disaster management tools for the Bay of Bengal and Indonesian regions, over a period of 7 years

From the mission statement, we derived several specifications to develop mathematical models that allowed us to define proper objectives and constraints. The mission should be focused on the observation of a well determined area on the globe. In particular, we identified a target delimited by latitudes 12°S and 20°N, and longitudes 75°E and 120°E. Further, the top-level requirements for a satellite mission in support of response and post-disaster operations are related to spatial resolution, coverage and revisit time, Martimort. Two classes of spatial resolution are considered strategic: 3 m and 30 m spatial resolution images both obtainable with Synthetic Aperture Radars (SARs) and optical payloads, Martimort De Bernardinis (2007), of which we will choose the latter. The objective of the analysis is now defined as to obtain the largest total target-area coverage (considering a fixed simulation time period for each design vector, i.e., 3 days), with the best possible image spatial resolution, and at minimum cost, see Table B.3. The ratio between the total coverage and the number of simulation days allows for estimating the average target-area coverage per day, and as a consequence providing a measure proportional to the average revisit time of the satellite over the entire target area.

The design variables needed for sizing the mission are shown in Table B.4. In Table B.5, the architectural variables and the levels they can assume are presented. The spatial resolution of the optical payload is linked to its physical dimensions and to the orbit by the following relationship, Wertz and Larson (1999b):

$$X_{nadir} = 2.44 \frac{h\lambda}{D} \quad (\text{B.1})$$

where X_{nadir} is the ground diffraction limited spatial resolution at the satellite nadir expressed in m, h is the altitude of the satellite above the nadir point expressed in m, λ is the wavelength of the radiation that we want to observe (≈ 0.5 m in the case of visible light). The variable D represents the aperture diameter of the optical instrument expressed in m. From Eq. (B.1) it can be concluded that the ground spatial resolution at nadir is higher (lower value of X_{nadir}) than the spatial resolution at the end of the swath width, because the distance from the satellite to the edge of the swath is larger. To compute the spatial resolution on the target area an average resolution has been taken into account for each satellite passage over the target area itself.

Objectives
Minimize mission cost [M \$ FY2010]
Maximize target area coverage [$\times 100\%$]
Minimize average spatial resolution on the target area [m at SSP]
Constraints
Satellite mass + adapter mass \leq launcher mass availability on orbit
Perigee altitude > 200 km
Spatial resolution ≤ 6 m at SSP
Downlink margin > 4 dB

Table B.3 Design Objectives and Constraints.

Design Variables		Code	Type	Intervals	
				Min	Max
Eccentricity	[-]	A	Continuous	0	< 1
Semi major Axis	[km]	B	Continuous	6400	42000
Inclination	[deg]	C	Continuous	0	180
Payload Aperture Diameter	[m]	D	Continuous	0.1	1
Satellite Transmitters Output Power (RF power)	[W]	E	Continuous	0	300
Satellite Aperture-Antenna Diameter	[m]	F	Continuous	0.1	1
Telemetry Data Rate	[Mbps]	G	Continuous	1	3
Type of Solar Cells	[-]	H	Architectural	1	3
Type of Batteries	[-]	I	Architectural	1	3
Payload TRL	[-]	J	Architectural	1	9
Launcher	[-]	K	Architectural	1	15

Table B.4 Design factors used in the simulation and relative design intervals.

Type of Solar Cells	Efficiency	Power Density [kg/W]
1-Silicon	14	115
2-Ga-As	24	140
3-Triple Junction	20	100
Type of Batteries	Energy Density [Wh/kg]	
1-Nickel-Cadmium	25	
2-Nickel-Hydrogen	35	
3-Lithium-Ion	140	

Payload TRL
Affects the cost of the payload for a given performance.

Launcher
The Launchers are selected from the database presented in Figure B.1.
Affects the mass available for a given orbit and the mission cost.

Table B.5 Architectural Variables. For more information on the type of solar cells, refer to Table A.3.

Lunar Space Station Mission Design

In this section the models and the assumptions for the design of the lunar space station mission are presented. The main mission objective of the study is to insert a manned space station in a low orbit around the Moon. The settings and the results for this applicative case are discussed by the author also in ?. The mathematical model of the lunar space station is discrete. This means that it is made of several types of space stations and delivery strategies, and each of these presents continuous design variables that characterize the behavior of the system. This mission is studied in Chapter 4 using global optimization. In Section C.1 the models of the building blocks of the space station are described. The various mission architectures, including type of space station and delivery strategy, are presented in Section C.2. In Section C.3, instead, we introduce the design variables used for the analysis, while in Section C.4 we discuss in details one of the objectives of the analysis, i.e., the value of the mission.

C.1 Scenario building blocks

The mathematical model of the lunar space station is developed considering two main system-architectures. The first one consists of a multi-element space station composed of two modules, i.e., a service module (SSSM, Space Station Service Module) and a node module (SSN, Space Station Node). The second one is a single-element space station, Skylab like. The SSSM provides electrical power, propulsion, guidance and control, communications capabilities, thermal control, and life support during all the mission phases of the space station. The SSN provides docking, berthing, and research (pressurized or not) capabilities. The SSSM is a rigid, cylindrical, element consisting of a pressurized and an unpressurized section. The pressurized section houses the pressurized avionic, the crew accommodation equipments, and part of the research equipments. These systems are located into racks and into the standoff volumes. The propulsion bay mainly accommodates the propulsion subsystem, i.e., the propellant tanks, the main engines and the sub-system control equipments. Other avionic equipments as the batteries, the communication equipments, and part of the power and GNC systems are located inside the non-pressurized avionic bay. The deployable solar arrays and radiators are externally mounted. The SSN is a rigid, cylindrical, pressurized element closed at the extremes by two conical segments. The SSN can accommodate up to six docking ports which are mounted at the edges of the cylindrical body of the SSN and on the lateral surface. The SSN accommodates eight racks that house the research equipment and the necessary avionic systems needed by the internal equipment and to support eventual additional systems attached to it. In Figure C.1(a) the on-orbit configuration of the multi element space station is represented. The Skylab-like space station consists of a single integrated module only (SSIM, Space Station Integrated Module). It provides electrical power, propulsion, guidance and control, communications capabilities, thermal control, and life support during all the mission phases, as well as docking, berthing, and research (pressurized or not also in this case) capabilities. The SSIM is very similar to the SSSM of the multi-element space station but it is longer to ensure the total required habitable volume. It also houses the docking ports. As the SSSM module, it has a cylindrical shape and it is divided into a pressurized and a non-pressurized section. The pressurized section houses the pressurized avionic systems, the crew accommodations, and the research equipments. All these elements are arranged into racks and standoff volumes. The SSIM can accommodate up to five

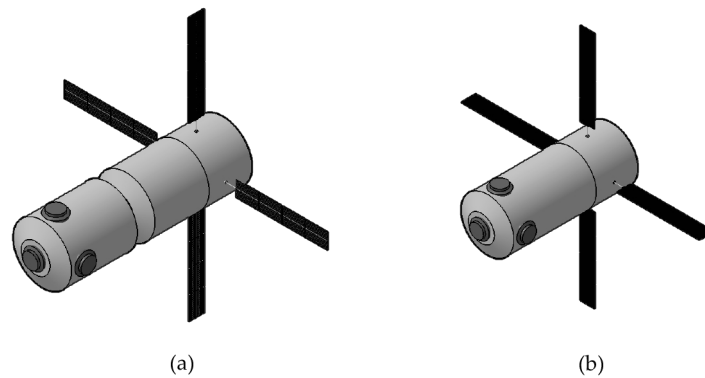


Figure C.1 Space station architectures. (a) Multi-element space station, (b) Integrated space station

docking ports which are mounted at the extremes of the cylindrical body and on the lateral surface, as shown in Figure C.1(b).

Thus, both the multi-element space station and the Skylab-like space station can ensure docking capabilities up to five visiting vehicles or generic support systems. The unpressurized section on the SSIM is located in the aft part of the module. The service compartment houses the non-pressurized avionic systems and the propulsion bays. The propulsion bays accommodate the propulsion sub-system, i.e., the propellant tanks, the main engines and the relative control equipments. The non-pressurized avionic bay accommodates avionic equipments, the batteries, the communication equipments and part of the power and GNC systems. The deployable solar arrays and radiators are mounted externally in correspondence of the non-pressurized avionic bay. In Figure C.1(b) the on orbit configuration of the Skylab-like space station is represented. Both the system architectures are designed to perform everyday station-keeping and on-orbit maneuvers using the propulsion system. In the following section, several mission scenarios regarding the deployment of the space station in low lunar-orbit will be presented. Some of the proposed mission scenarios foresee that the orbit maneuvers are performed by the space station modules themselves, while some of them foresee that the orbit maneuvers are performed by a transfer module (TM). The TM is a propulsion module that provides the necessary thrust to leave the initial orbit and inject the payload into the target orbit. The external shape of the transfer module is cylindrical. The length of the TM module is proportional to the propellant tank length. The propellant tank dimensions are computed as a function of the propellant mass which is proportional to the required ΔV and to the total mass that the propulsion system must accelerate. The structure of the TM consists of an unpressurized structure with dedicated tank supports. The unpressurized structure provides structural support to the other subsystem components as secondary propulsion devices, power and avionic equipments and ensures the proper interface with the launcher and the payload.

C.2 Mission architectures

A single-element or multi-element space station can be deployed in a low lunar-orbit according to a large variety of mission architectures. In fact, considering all the possible combinations of number and type of building blocks, one can think of many different solutions to the problem. In this section, some of the possible mission architectures are described. The type of mission architectures considered in this thesis is neither exhaustive nor complete. They are examples used to demonstrate how and to what extent optimization methods could help the engineering team in reducing the number of feasible solutions to analyze, even for a complex system as a lunar-orbiting space station.

Three mission architectures have been considered for the deployment of the Skylab-like space station and seven mission architectures have been considered for the deployment of the multi-element space station. The building blocks considered for all the mission architectures are listed in Table C.1.

The mission architectures considered for this study foresee two main mission-nodes. The first node is near the Earth, in Low Earth Orbit (LEO), while the second one is in the cis-lunar space. This node is called Low Lunar Orbit and it represents the orbit where we want the space station to be in its final configuration. All the mission architectures begin by launching the building blocks in LEO. The first





Description	Acronym	Symbol
Space station integrated module	SSIM	
Space station service module	SSSM	
Space station node	SSN	
Transfer module	TM	

Table C.1 Description of the main building blocks.

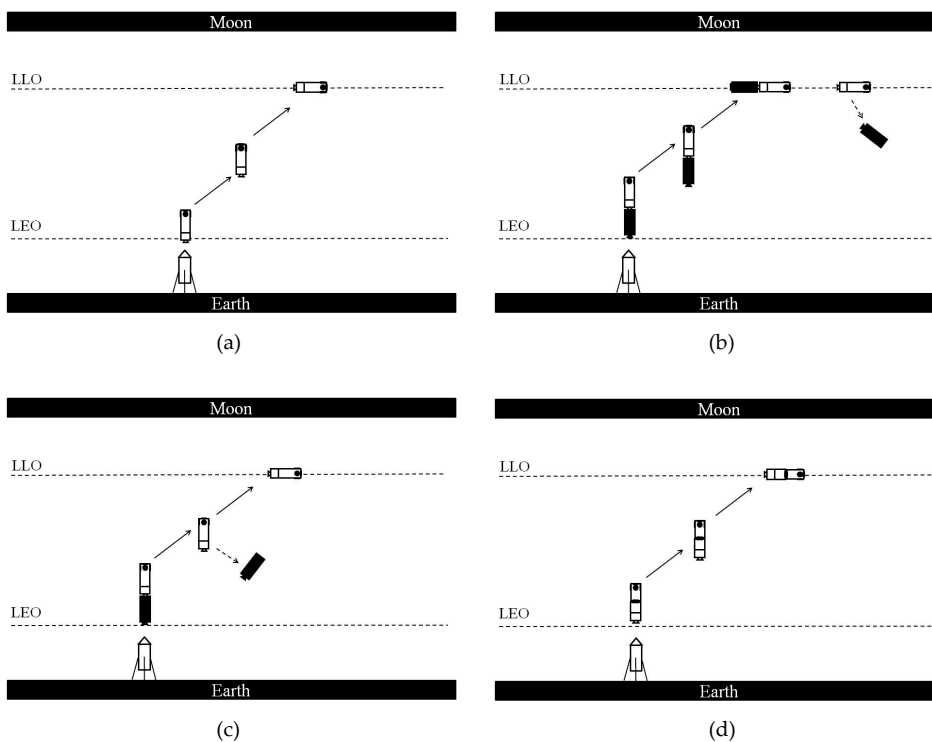


Figure C.2 Space-station deployment mission architectures.

mission architecture is presented in Figure C.2(a). This mission architecture is only made of a single building block, i.e., the SSIM. Once the SSIM is inserted in LEO, it performs the Trans-Lunar Injection (TLI) and Lunar Orbit Injection (LOI) maneuvers. The mission scenario does not foresee any staging or Rendezvous and Docking (R & D). The second mission architecture (see Figure C.2(b)) foresees two building blocks. The SSIM and the TM are inserted on orbit by one or two launches. Once in orbit, the systems perform the TLI and LOI maneuvers, in a docked configuration. Unlike the first mission architecture, the maneuvers are not performed by the SSIM. Indeed, they are performed by the TM. Once the TLI maneuver is completed the TM is discarded. The building blocks considered for the third mission architecture are the SSIM and the TM, as in the previous one. In this case the TM module performs the TLI maneuver only. Once the TLI is completed, the TM is discarded and the SSIM performs the LOI maneuvers using its own propulsion system. This mission architecture is presented in Figure C.2(c). The fourth mission architecture (see Figure C.2(d)) is very similar to the first one. The SSSM and the SSN are inserted on orbit by one or two launches. In case of the two-launches mission, the R & D of the two modules is completed in LEO. Once the systems are in LEO, the SSSM performs the TLI and LOI maneuvers. As for the first mission architecture, this mission does not foresee staging and the R & D (if needed) is completed in LEO.

The number of building blocks increases to three considering the mission architecture of Figure

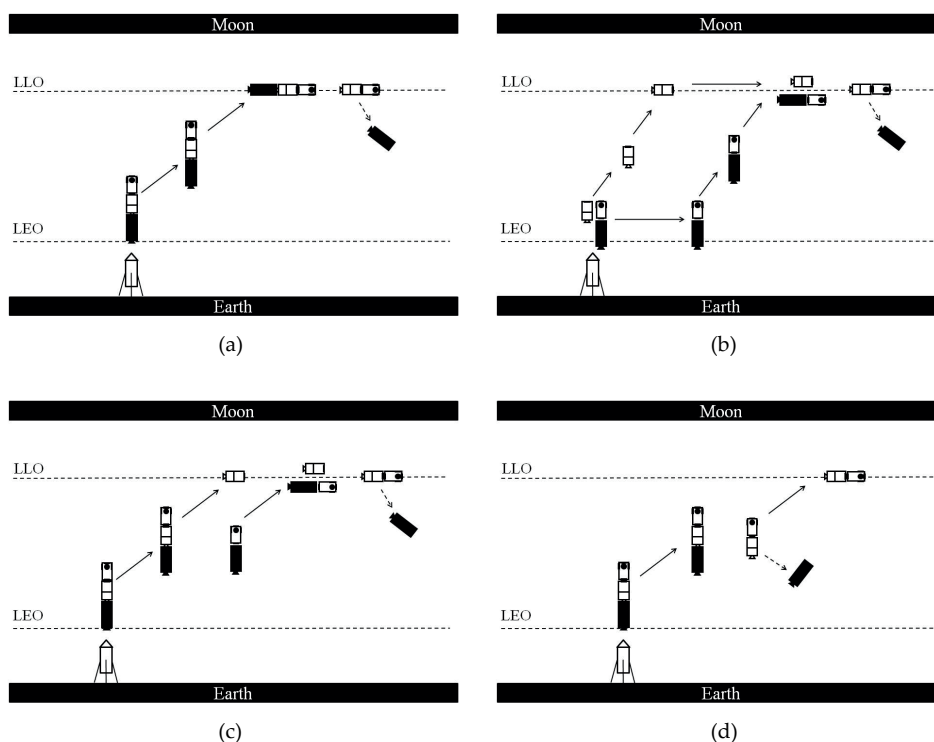


Figure C.3 Space-station deployment mission architectures. Continued.

C.3(a). The mission begins when the SSSM, the SSN, and the TM are docked together in LEO. If a one-launch solution is considered, the building blocks are launched in the docked configuration. If the two-launch solution is considered, instead, the first launcher inserts the SSSM on orbit while the second launcher inserts the TM and the SSN modules docked together on orbit. This one-launch or two-launches configurations will be considered for all the remaining mission architectures. The two-launch solution foresees R&D in LEO. Once all the systems are docked in LEO, this mission architecture foresees that the TM performs the TLI and LLO insertion maneuvers, and it is discarded at the end.

In the architecture of Figure C.3(b), the one-launch or two-launches solutions are possible. Once on orbit, the SSSM performs the TLI and LOI maneuvers. When the SSSM is in LLO, the mission of the SSN and TM begins. The TM performs the TLI and LLO injection maneuvers and at the end of these, it is discarded. Once the SSSM and SSN are in LLO a R&D maneuver is performed to finally assemble the space station. According to the mission architecture of Figure C.3(c), the mission begins with the TM module providing the necessary acceleration to reach the TLO to the SSSM and the SSN. Once the systems are accelerated, the undocking of the SSSM occurs. The SSSM and the SSN-TM assembly reaches LLO separately. The TM is discarded when the necessary SSSM-SSN docking maneuvers are completed. The mission architecture of Figure C.3(d), foresees that once the TM, the SSSM, and the SSN perform the TLI maneuver docked together, the TM module is discarded and the SSSM provides the ΔV needed to reach the LLO. The last two architectures foresee the utilization of two TMs. The first TM is docked to the SSSM and the second one is docked to the SSN. The mission starts when TM puts the SSSM in TLO and then in LLO. When the SSSM reaches LLO the first TM module is discarded and the mission of the SSN begins. The second TM performs the TLO and LLO injection maneuvers and then it is discarded. Once the SSSM and the SSN are in LLO, they perform a docking maneuver. In the last mission architecture the first TM, which is attached to the SSSM, is discarded at the end of the TLO injection maneuver and the SSSM performs the LLO injection maneuver. Once the SSSM reaches the LLO, the mission continues as described already for the mission architecture of Figure C.4(a). The second TM inserts the SSN in TLO and than in LLO. It is discarded at the end. Finally, the SSSM and the SSN perform a docking maneuver.

The ΔV for the maneuvers considered for the mission architectures described before are 3,120 m/s for the LEO-TLO transfer, and 1,390 m/s for the TLO-LLO transfer. In this study, the design and opti-

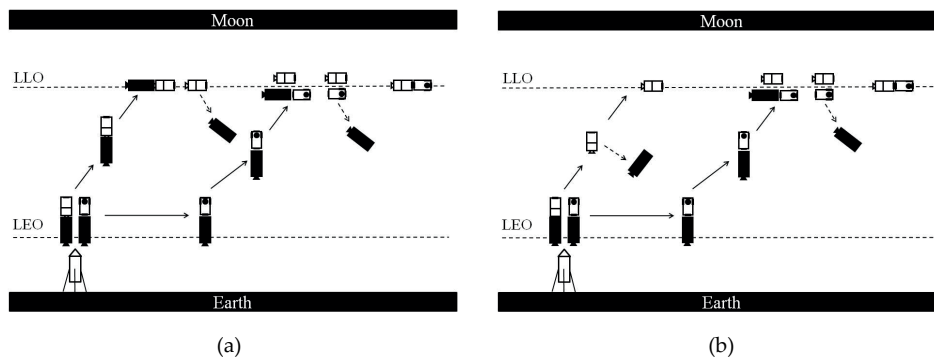


Figure C.4 Space-station deployment mission architectures. Concluded.

Design Variables	Code	Type	Intervals		Levels	
			Min	Max		
Type of Mission	[-]	A	Disc.	1	10	10
# of Launches	[-]	B	Disc.	1	2	2
# of Crew members	[-]	C	Disc.	3	6	4
Volume distribution	[-]	D	Cont.	40%	60%	–
Node/SM						
# of Hatches SM	[-]	E	Disc.	1	5	5
# of Hatches Node	[-]	F	Disc.	1	5	5
# of Hatches IM	[-]	G	Disc.	1	5	5
SM Diameter	[m]	H	Cont.	3.5	5.5	–
Node Diameter	[m]	I	Cont.	3.5	5.5	–
IM Diameter	[m]	J	Cont.	3.5	5.5	–
# of Racks SM	[-]	K	Disc.	4	10	7
# of Racks Node	[-]	L	Disc.	4	10	7
# of Racks IM	[-]	M	Disc.	6	18	13
Moon Orbit Altitude	[km]	N	Cont.	80	150	–
Mission Duration	[days]	O	Cont.	25	35	–
ISP SM	[s]	P	Cont.	250	350	–
ISP IM	[s]	Q	Cont.	250	350	–
Min. Habitable Volume	[m ³]	R	Cont.	35	45	–
Racks SM mass	[kg]	S	Cont.	160	200	–
Racks Node mass	[kg]	T	Cont.	160	200	–
Racks IM mass	[kg]	U	Cont.	160	200	–
Max. Power Required SM	[kW]	V	Cont.	8.5	11.5	–
Max. Power Required IM	[kW]	W	Cont.	8.5	11.5	–
ISP TM	[s]	X	Cont.	350	450	–

Table C.2 Design factors used in the simulations and relative design intervals.

mization of the Earth-Moon trajectory was not taken into account. Standard values for the required ΔV were considered instead.

C.3 Design variable settings

The design variables taken into account for the analysis presented in this thesis are described in Table C.2.

The *type of mission* design variable allows choosing amongst one of the ten mission architectures described in the previous section. Each mission architecture foresees a specific number and type of modules, a combination of orbit maneuvers and staging phases. All these mission features characterize the mission architecture with pros and cons. If the number of docking and undocking maneuvers increases, for instance, the mission-success ratio (described later) decreases. In this case, however, the entire mission results more flexible. As said already, each mission architecture can be deployed using

one or two launches. The variable *# of Launches* allows choosing between the one-launch solution and the two-launch solution. If the one-launch solution is selected, all the building blocks are launched in the docked configuration. As a consequence, on-orbit docking maneuvers are avoided but the launcher payload mass increases. If the two-launch solution is chosen, instead, the launcher payload mass and the launcher cost decrease. In this case the launch reliability increases but on-orbit docking maneuvers became necessary, with the consequence that the mission-success ratio decreases.

The *# of Crew members* represents the number of astronauts that the space station can support. The number of crew members ranges between a minimum of 3 astronauts to a maximum of 6 astronauts. If the number of crew members increases the habitable volume that must be guaranteed on the space station increases. A larger space station becomes also heavier and more expensive. The variable *Volume distribution Node/SM* is related to the multi-element space station architecture. This variable defines how much habitable volume is allocated to the SSSM and how much on the SSN. The allocation of more or less habitable volume to one module influences the module characteristics as the external layout and the mass proprieties. The variables *# of Hatches SM*, *# of Hatches Node* and *# of Hatches IM* are the number of hatches on the SSSM, on the SSN and on the SSIM. The number of hatches influences the mass proprieties of the systems and it is representative of the capability of the space station to support more or less visiting/additional vehicles. It is also an indicator of the scalability of the space station itself. The variables *SM Diameter*, *Node Diameter* and *IM Diameter* are the external diameter of the SSSM, of the SSN and of the SSIM, respectively. If the modules of the multi-element space station have different external diameters, the space station cost increases because the production cost increases. The model considers the additional cost as exponentially-increasing with the modules diameter difference. The variables *# of Racks SM*, *# of Racks Node* and *# of Racks IM* are the number of racks that can be stored on the SSSM, the SSN and the SSIM, respectively. The racks provide accommodation to part of the space station subsystems (i.e. life support systems and crew accommodation) and to experimental equipments. If the number of racks is at the minimum value, this implies that volume dedicated to experimental equipments is also reduced. The *Moon Orbit Altitude* is the altitude of the space station orbit around the Moon. The orbit altitude influences the power subsystem, amongst the others. The *Mission Duration* is related to the crew mission-duration inside the space station. A large mission duration implies a large habitable volume that must be guaranteed on the station to comply with the necessary comfort levels.

Moreover, the mission duration influences the amount of consumables that must be stored on board of the space station. The *ISP SM*, *ISP IM* and *ISP TM* are the specific impulses of the SSSM, SSIM and TM propulsion-system propellants, respectively. The value of these design variables is related to the propulsion technology adopted by each specific building block. If the specific impulse increases, the amount of necessary propellant mass decreases. Further, the mathematical model takes into account also the fact that if the modules have different propellants, the total production costs increase. This is due to the consideration that different infrastructures for propellant managing are necessary. The *Min. Habitable Volume* variable is representative of the minimum habitable volume that the space station must guarantee. The *Racks SM mass*, *Racks Node mass* and *Racks IM mass* are the mass of the rack of the SSSM, the SSN and the SSIM, respectively. The *Max. Power Required SM* and the *Max. Power Required IM* are the maximum power required by the power system of the SSSM and by the SSIM, respectively.

C.4 The value of the mission

A standard recipe to evaluate a space mission does not exist. As reported by Larson (1999), if the possible mission options have equal or similar performances the selection of the best one can be based on the mission cost. On the other hand, if the mission options imply different performances and success ratio, the comparison of the alternative mission concepts becomes more challenging. Nevertheless, the space-mission value-analysis can create the basis to compare different architectures. Once the necessary system functions have been established, the value analysis allows the definition of the cost-effectiveness (or value, V) of a mission by dividing the system global functionality (f) by its cost (C) and multiplying by the mission success ratio (p).

$$V = \frac{f}{c}p \quad (\text{C.1})$$

To implement the value analysis to the previously described mission scenarios, the following space mission functionalities have been identified as the most important and representative of the system:

- The pressurized volume of the space station (V_p) is representative of the capabilities of the system to accommodate a crew. If the pressurized volume increases the space station offers a higher level of comfort, or it is able to accommodate a larger number of astronauts, or it is able to support astronauts for a longer period of time. The pressurized volume of the space station is also indicative of the research potentialities of the system. The *research potentialities* of the space station can be considered proportional to the pressurized volume that can be allocated to the experimental equipments.
- The number of crew members (n_c) that the space station can support and their maximum allowed permanence time on-board, t_m , are representative, amongst other factors, of the research capabilities on board of the station. Further, a larger number of crew members and a larger permanence time could allow for more maintenance and operations (in general) capabilities of the space station.
- The number of hatches (n_h) of the space station is representative of the capability of the space station to support more or less visiting vehicles and to be expandable.
- The racks provide research equipments accommodation. Therefore, with an increasing number of racks (n_r) and their total mass (m_r), the potentialities for research increase as well.

The indicator representative of the system global functionality, f can be obtained by the sum of each system function multiplied by a proportionality factor. The proportionality factors ($\alpha_1, \alpha_2, \dots, \alpha_n$) indicates the relative importance of the system functions.

$$f = \alpha_1 V_p + \alpha_2 n_c + \alpha_3 t_m + \alpha_4 n_h + \alpha_5 n_r + \alpha_6 m_r \quad (C.2)$$

Space-system costs cannot be estimated with a high level of confidence, especially in the early design phases. This is because in the aerospace field a mass-production does not exist and because the knowledge of the production costs of the existing products is classified most of the times. As a consequence, the traditional cost models assume costs proportional to mass and system complexity. The method implemented and adopted to estimate the building-blocks cost is based on the Advanced Missions Cost Model (AMCM) proposed by NASA, Larson (1999), NASA (2011). This cost model is a parametric model suitable for manned space systems and useful to estimate development and production costs of the spacecraft. The AMCM is not only based on the mass, but it takes also the type of system (manned habitat, manned re-entry, planetary lander, etc.), the level of design inheritance of the system, the level of programmatic and technical difficulty anticipated for the new system, and the total number of units that will be produced into account. The cost model is based on a database of more than 260 space programs, NASA (2011). The equation used to estimate the cost is the following:

$$C = \alpha Q^\beta \cdot M^\Theta \cdot \sigma^S \cdot \epsilon^{\frac{1}{1000-1900}} \cdot B^\phi \cdot \gamma^D \quad (C.3)$$

where the cost regression coefficient α is equal to $5.04839E - 4$, β is equal to 0.594183076, Θ is equal to 0.653947922, δ is equal to 76.99939424, ϵ is equal to $1.68051E - 52$, ϕ is equal to -0.355322218 and γ is equal to 1.554982942. The IOC is the year of Initial Operating Capability and for space systems, this is the year in which the spacecraft or vehicle is first launched. Q is the development and production quantities of the system expressed in equivalent unit, while M is the dry mass of the system in Pounds. The parameter S is the Specification. It designates the type of mission that is going to be flown (e.g., planetary, physics and astronomy, Earth observation). The parameter B is the system's block number, which represents the level of design inheritance. It is equal to 1 if the design is completely new while it is equal to 2 or more if the design is derived by an existing one. Finally, D is a qualitative assessment of the relative programmatic and technical development and production complexity of the element. It may range between -2.5 (design extremely easy) to 2.5 (design extremely complex).

The mission success ratio (p) is an indicator that is proportional to the probability of mission success. The mission success ratio is proportional to the launches and docking/undocking success probability. The launcher model, which is based on a database of about fifty current launch vehicles, Advameg (2011), estimates the launch probability of success (as well as the launch cost) on the basis of the launcher payload mass. The statistical survey shows that the higher is the launcher payload mass, the higher is the launch costs and the lower is the probability of mission success. The probabilities of docking/undocking success as well as the reliability of the space building blocks have been assumed constant. The mission success-ratio model takes into account the number of launches and the number of R&D ($n_{R\&D}$). It evaluates the mission success-ratio (p) by multiplying the launch probability-of-success (p_l) by the R&D probability of success ($p_{R\&D}$). The equation used is the following:

$$p = p_l (p_{R\&D} \cdot n_{R\&D}) \quad (\text{C.4})$$

Appendix *D*

Atmospheric Entry Vehicle

D.1 Capsules geometry

The capsules that will be used in this study belong to the family of the Apollo-like capsules. These are axial-symmetric capsules that can be defined by 5 parameters:

- Nose radius, R_N
- Side radius, R_S
- Rear part half angle, θ_C
- Mid radius, R_m
- Rear part length, L_C

A schematic representation of these parameters is shown in Figure D.1. This parametrization consists of four matched analytical geometries, namely a sphere segment, a torus segment, a conical frustum and again spherical segment at the back. Since the shape is axial-symmetric, the entire surface geometry is defined by the cross-section shown in Figure D.1.

The shift of the center of gravity in the vertical and longitudinal direction are additional variables that may be taken into account in the optimization process. However, as demonstrated by Dirkx (2011), the shift in the longitudinal direction does not have a significant effect on the static stability properties and the dynamic behavior of the capsules. Therefore only the shift in the vertical direction (ΔZ_{cog}) will be used as design parameter.

The following two constraints must hold for the capsule to have a feasible shape:

$$\begin{aligned} R_m &< R_M \\ L_c &< \frac{R_m - R_s (1 - \cos \theta_C)}{\tan \theta_C} \end{aligned} \quad (D.1)$$

D.2 Material properties

In this section we present the thermo-physical properties of the materials used to obtain the results presented in this paper. All the TPS solutions are obtained with an external skin, an intermediate layer of Saffil insulating material with the thickness of 100 mm, and an internal structure of Titanium with the thickness of 3 mm. The materials for the insulation layer and the internal structure and their thickness are not part of the optimization. They are equal for all the TPS solutions used in this paper.

D.2.1 Metallic TPS solutions

In Table D.1 the thermo-physical properties of the PM2000, Saffil insulator, and Titanium are listed. The density of Saffil insulation and Titanium are 96 and 4500 kg/m³, respectively. The properties of insulation used here are the effective properties which assume porous insulation material to be isotropic

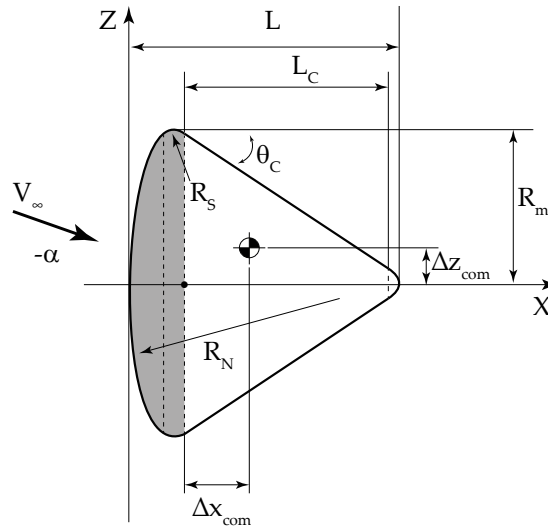


Figure D.1 Schematic representation of the geometrical parameters of the capsules. The gray area is the nose of the capsule, the white area is the rear part. Adapted from Hirschel and Weiland (2009).

and homogeneous material (Liu and Zhang, 2011). The density of the PM2000 is 7180 kg/m^3 , its melting point is 1756 K while the maximum service temperature is 1623 K . The temperature of 1200 K is considered the limit for full re-usability of PM2000.

T [K]	C_p [J/g K]	k [W/mK]
273	0.724	0.025
373	0.950	0.034
473	0.1022	0.043
573	0.1093	0.053
673	0.1139	0.065
773	0.1172	0.078
873	0.1197	0.092
973	0.1223	0.108
1073	0.1239	0.126
1172	0.1252	0.146
1273	0.1260	0.167
1373	0.1269	0.191
1473	0.1273	0.217

Table D.1 Materials thermo-physical properties. PM2000 (left)(Plansee, 2012), Saffil insulator (right)(Liu and Zhang, 2011).

The validation of the thermal model was performed with the material PM1000. PM1000 was used in the original publication, but since it is not in production anymore, we decided to use the PM2000 for the actual robust-optimization process described in this paper.

The density of PM1000 is 8240 kg/m^3 . The following relationships are valid for the thermal conductivity and the specific heat of the PM1000:

$$\begin{aligned}
 k_{PM1000} &= 0.025333 \cdot (T - 273.15) + 11 \text{ [W/mK]} \\
 &\text{for } 273.15 \text{ K} < T \leq 1023 \text{ K} \\
 k_{PM1000} &= 0.026667 \cdot (T - 1023) + 30 \text{ [W/mK]} \\
 &\text{for } 1023 \text{ K} < T \leq 1470 \text{ K} \\
 C_{pPM1000} &= 0.408333 \cdot T + 410 \text{ [J/kgK]} \\
 &\text{for } 273.15 \text{ K} < T < 1470 \text{ K}
 \end{aligned} \tag{D.2}$$

T [K]	C _p [J/g K]	k [W/mK]
293	0.544	16.33
373	0.544	16.33
473	0.628	16.33
573	0.670	16.75
673	0.712	17.17
773	0.754	18.00
873	0.837	18.00

Table D.2 Materials thermo-physical properties. Titanium (Liu and Zhang, 2011).

The metallic TPS solutions also present water as cooling mechanism. The density of the water is 1000 kg/m^3 , its heat of evaporation is 2260000 J/kg . The following relationships are valid for the conductivity and specific heat as a function of the temperature, provided in Kelvin:

$$k_{H_2O} = -0.7676 + 7.536 \cdot 10^{-3}T - 9.825 \cdot 10^{-6}T^2 \text{ [J/mK]} \quad (\text{D.3})$$

$$C_{pH_2O} = (917.5 - 10.1016 \cdot T + 0.0454134 \cdot T^2 - 9.07517 \cdot 10^{-5}T^3 + 6.8070 \cdot 10^{-8}T^4) / 0.018 \text{ [J/kgK]} \quad (\text{D.4})$$

In case of direct water cooling solution, when the temperature of the water reaches the boiling limit, the heat from the skin is absorbed by the water for its evaporation leaving the temperature of the skin at a constant value. Therefore, the water consumption can be expressed as follows:

$$F_{H_2O} = \frac{q_{Aero} - q_{Rad}}{H_{evaporation}} \text{ [kg/sm}^2\text{]} \quad (\text{D.5})$$

The assumption is that the water is cooling through nucleate boiling. Therefore we consider the temperature of the innermost skin, which is in contact with the water, being at the same temperature of the water itself. When the enhanced-radiation cooling is adopted, the cooling principle is still based on evaporation but the engineering solution is substantially different, see Figure D.2. Water is contained in a porous material, ZAL-15 for instance (a mixture of Alumina 85 % and Silica 15%) that is detached from the external skin. At the interface the heat is transferred through radiation, therefore, equilibrium between the innermost layer of the skin and the ZAL-15 shall be taken into account in the transient model. The water consumption and temperature of the porous material can be computed with the following relationships, where σ indicates the thickness of the porous material and \dot{m} the evaporating water flux (Buursink, 2005):

$$\Delta T_{H_2O} = \begin{cases} \frac{q_{in}}{\rho_{H_2O} \cdot \sigma \cdot C_{pH_2O}}, & \text{if } T_{H_2O} < T_{boil} \\ 0, & \text{if } T_{H_2O} = T_{boil} \end{cases} \quad (\text{D.6})$$

$$= \begin{cases} 0, & \text{if } T_{H_2O} < T_{boil} \\ \frac{q_{in}}{H_{evaporation}}, & \text{if } T_{H_2O} = T_{boil} \end{cases}$$

D.2.2 Ceramic TPS solutions

The UHTC material used in this paper is the ZrB₂-SiC. The high-enthalpy test facility of CIRA conducted several experiments on this heat-resistant material, thus some information is available in literature (Francese, 2002). The density of the ZrB₂-SiC is 5610 kg/m^3 . Its melting temperature is 3020 K , the maximum temperature for single utilization of the material is 2860 K , while it can be reused multiple times is the maximum temperature does not exceed 2300 K . In Table D.3 the thermo-physical properties of the ZrB₂-SiC are presented.

D.2.3 Ablative TPS solutions

The process related to the ablation is very complex to model. In this paper we adopted a simplified approach to take into account the two main phenomena related to the ablation, *i.e.*, the pyrolysis, at

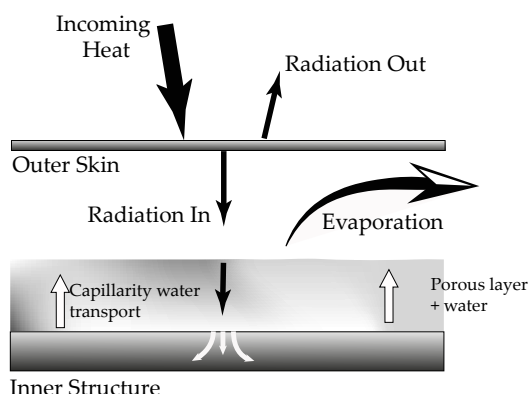


Figure D.2 Enhanced Radiation Cooling TPS, schematic representation.

T [K]	C _p [J/g K]	T [K]	k [W/mK]	T [K]	ε
298	0.459	300	103.8	1037	0.775
300	0.462	900	83.07	1169	0.712
400	0.554	1500	76.15	1263	0.72
500	0.603	2100	69.23	1334	0.734
600	0.633	2400	67.50	1485	0.748
700	0.656	-	-	1681	0.724
800	0.673	-	-	1842	0.663
900	0.687	-	-	-	-
1000	0.699	-	-	-	-
1100	0.711	-	-	-	-
1200	0.721	-	-	-	-
1300	0.731	-	-	-	-
1400	0.741	-	-	-	-
1500	0.750	-	-	-	-
1600	0.759	-	-	-	-
1700	0.768	-	-	-	-
1800	0.776	-	-	-	-
1900	0.785	-	-	-	-
2000	0.794	-	-	-	-
2100	0.802	-	-	-	-
2200	0.811	-	-	-	-

Table D.3 Thermophysical properties of the ZrB₂-SiC.

the interface between charred and uncharred material, and the charring at the external interface. These two additional fluxes are taken into account in the model as explained in Section 5.4.4 regarding the *interface node* and the *external node* respectively. The materials thermo-physical properties presented in this section are derived from the work of Delgado Montes (1989) concerning the Phenolic Nylon. The Carbon Phenolic properties are adapted from the work of Sutton (1970), while the PICA properties are adapted from Parmenter *et al.* (2001) and Tran *et al.* (1996). At the outer surface of an ablative TPS several phenomena take place: conduction inwards and radiation outwards of the incoming heat, but also sublimation of the charred material and blockage due to the mass transfer of material in the boundary layer. The *cooling flux* of Eq. (5.16) and Eq. (5.17) at the external surface of an ablative TPS is equal to $\dot{m}_c \cdot H_{Subl}$. H_{Subl} is the heat of sublimation, \dot{m}_c is the mass removal rate of the char material:

$$\dot{m}_c = \begin{cases} \frac{1}{H_{Subl}} \left(T_i^t - T_i^{t-1} \cdot \frac{2k_i \Delta t}{\rho C_p \Delta y^2} - \right. & \text{if } T_i^{t-1} \geq T_{Subl} \\ \left. - T_{i+1}^{t-1} \cdot \frac{2k_{i+1} \Delta t}{\rho C_p \Delta y^2} \right) \frac{\rho C_p \Delta y}{2\Delta t} - q_{Aero} + \sigma \epsilon (T_i^{t-1})^4 & \\ \\ \frac{1}{2} \left(- \frac{(h_e - h_w) K^2 P_w}{q_{Aero} \lambda N^{0.6}} + \right. & \text{if } T_i^{t-1} < T_{Subl} \\ \left. + \sqrt{\left(\frac{(h_e - h_w) K^2 P_w}{q_{Eff} \lambda N^{0.6}} \right)^2 + 4K^2 P_w C_e} \right) & \end{cases} \quad (D.7)$$

The incoming heat flux that should be considered is the effective heat flux, q_{Eff} , which is computed taking into account the blockage effect:

$$q_{Eff} = \alpha q_{rad} + q_{conv} \left(1 - \frac{h_w}{h_e} \right) \cdot \left[1 - \left(\frac{0.724 h_e}{q_{conv}} (\alpha_c \dot{m}_c + \alpha_p \dot{m}_p) - 0.13 \left(\frac{h_e}{q_{conv}} \right)^2 (\alpha_c \dot{m}_c + \alpha_p \dot{m}_p)^2 \right) \right] \quad (D.8)$$

Here q_{rad} and q_{conv} represent the radiative and convective fractions of the incoming heat flux respectively. The symbols h_e and h_w represent the environmental and wall enthalpies, while α_c and α_p represent the transpiration effectiveness of char mass loss and pyrolysis products respectively.

At the interface between charred and uncharred material, the pyrolysis cooling flux is modeled as $\dot{m}_p \cdot H_{Pyro}$, where H_{Pyro} is the heat of pyrolysis, \dot{m}_p is the mass flux of the pyrolysis material:

$$\dot{m}_p = \left\{ T_i^t - \frac{2\Delta t}{\rho_i C_{p_i} \Delta y_i + \rho_{i+1} C_{p_{i+1}} \Delta y_{i+1}} \left[\frac{k_i}{\Delta y_i} T_{i-1}^t + \frac{k_{i+1}}{\Delta y_{i+1}} T_{i+1}^t \right] - \left[1 - \frac{2\Delta t}{\rho_i C_{p_i} \Delta y_i + \rho_{i+1} C_{p_{i+1}} \Delta y_{i+1}} \left(\frac{k_i}{\Delta y_i} + \frac{k_{i+1}}{\Delta y_{i+1}} \right) \right] T_i^{t-1} \right\} \cdot \frac{-(\rho_i C_{p_i} \Delta y_i + \rho_{i+1} C_{p_{i+1}} \Delta y_{i+1})}{2\Delta t H_{Pyro}} \quad (D.9)$$

In case $T_i^{t-1} < T_{Pyro}$, the mass flux of the pyrolysis material is zero. The quantities needed to model the ablative TPS, for the three types of ablative materials considered here, are shown in Table D.4. The symbols ρ , C_p , and k represent the density, specific heat and conductivity, respectively. The symbol ϵ is the emissivity, while A , B , and D represent the reaction rate, activation energy, and diffusion coefficient respectively. P_w is the environmental pressure at the outer edge of the boundary layer, C_e is the oxygen concentration, and λ is the weight of char removed per unit weight of oxygen. The factor K is computed as $Ae^{-B/T}$.

The Phenolic Nylon ablative material presents a specific heat that varies with temperature according to the following law: $764.04 + 2.812 \cdot T$ $J/kg \cdot K$ in the uncharred form. For the charred Phenolic Nylon we considered a constant specific heat equal to 800 $[J/kg \cdot K]$. Its conductivity is equal to $0.7 + T \cdot 3.457E - 5$ W/mK when uncharred. The charred Phenolic Nylon presents a conductivity equal to 2 W/mK .

D.3 Validation of the thermal models

In this section, we present the results of the validation of the thermal model described in Section 5.4.4, for the TPS solutions implemented in the analysis presented in this paper.

		Phenolic Nylon	Carbon Phenolic	PICA
ρ_{unchar}	[kg/m ³]	553	1392	266
ρ_{char}	[kg/m ³]	143	1184	210
ϵ	[-]	0.8	0.7	0.9
A	[kg/m ² .sec.atm]	4.9E10	4.9E10	4.9E10
B	[K]	4.25E4	4.25E4	2.25E4
D	[m ² /s]	0.85	0.85	0.85
T_{subl}	[K]	1872	3030	3700
T_{pyro}	[K]	945	945	1973
ΔH_{subl}	[J/kg]	5E7	20.88E6	0.25E9
ΔH_{pyro}	[J/kg]	1.28E6	0.465E6	0.5E6
C_e	[-]	0.23	0.23	0.23
λ	[-]	0.75	0.75	0.75
h_e	[J/kg]	3.1E6	3.1E6	3.1E6
α_c	[-]	0.2	0.2	0.2
α_p	[-]	0.1	0.1	0.1

Table D.4 Ablative materials thermo-physical properties.

Uncharred			Charred			Uncharred			Charred	
T	C_p	k	T	C_p	k	T	C_p	k	C_p	k
256	0.99	0.561	278	1	0.81	256	0.879	0.0397	0.733	0.0397
311	1.22	0.639	556	1.38	0.872	294	0.984	0.0402	0.783	0.0402
367	1.33	0.693	811	1.61	0.935	444	1.298	0.0416	1.093	0.0416
422	1.39	0.742	1089	1.86	0.977	556	1.465	0.0453	1.319	0.0453
477	1.45	0.774	1366	2.01	1.128	644	1.570	0.0470	1.432	0.0470
533	1.51	0.774	1645	2.06	1.189	833	1.716	0.0486	1.674	0.0486
589	1.56	0.742	1923	2.11	1.502	1111	1.863	0.0523	1.842	0.0523
644	1.62	0.698	2200	2.15	2.065	1389	1.934	0.0560	1.967	0.0560
700	1.68	0.630	2478	2.17	2.790	1667	1.980	0.0698	2.051	0.0605
811	1.80	0.479	2756	2.19	3.502	1944	1.988	0.0872	2.093	0.0729
-	-	-	3030	2.21	4.88	2222	2.001	0.111	2.11	0.0922
-	-	-	3311	2.24	6.39	2778	2.009	0.175	2.135	0.146
-	-	-	3590	2.26	7.38	3333	2.009	0.278	2.152	0.223
-	-	-	3867	2.28	9.325	-	-	-	-	-

Table D.5 Materials thermo-physical properties, as a function of temperature. Carbon Phenolic(left), PICA(right). Temperature in [K], C_p in [J/g K], k in [W/mK]

D.3.1 Metallic uncooled TPS, hot structure approach

The TPS used for the validation of the model is made of an external layer of PM2000 10mm thick. A layer of Saffil insulator with thickness of 50mm is added after, and the internal structure is made of a 5mm Titanium layer. The comparison with the results obtained by Liu and Zhang (2011) are presented in Figure D.3. There, it can be observed that there is almost a perfect match between the benchmark and the computed temperature trends for the outer skin and the innermost layer of the TPS.

D.3.2 Metallic cooled, nucleate boiling and enhanced-radiation cooling approaches

For the validation of the TPS model with cooling mechanisms a capsule with nucleate-boiling at the nose and enhanced-radiation cooling at the rear part is considered. The capsule experiences the heat fluxes presented in Figure D.4(a). The computed and the benchmark temperature profiles are very close to each other as evident from Figure D.4(b), where also the comparison with the case of a capsule uncooled rear-part is plotted. In Figure D.4(c), the water consumed to cool down the nose and the rear part is visualized. The results have been obtained with a PM2000 external skin of 1mm thickness for both nose and rear part. The heat fluxes and the benchmark temperatures are these of the DART capsule, a re-entry test vehicle developed at Delft University of Technology (Buursink, 2005).

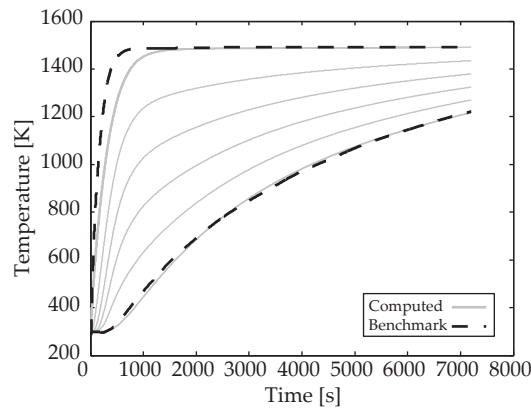


Figure D.3 Metallic uncooled TPS, temperature profiles. Incoming heat-flux $240kW/m^2$.

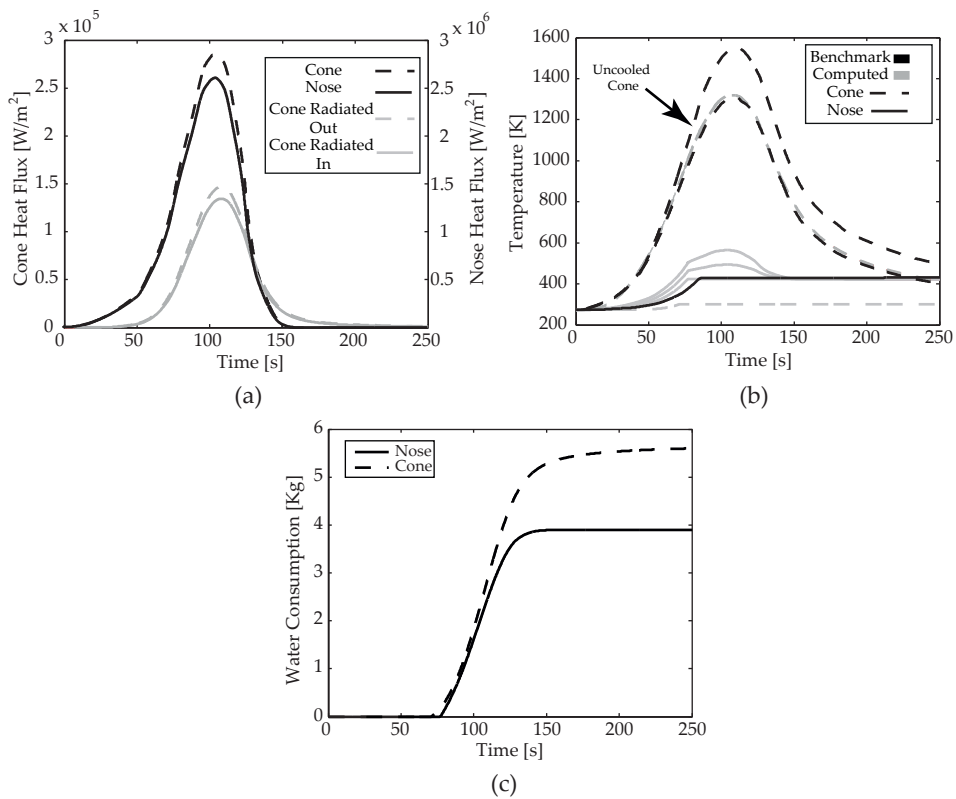


Figure D.4 Metallic cooled TPS. (a) Incoming heat fluxes; (b) comparison between benchmark and computed temperatures; (c) Cooling-water consumption.

D.3.3 Ceramic TPS

The performance of the thermal model with the UHTC ZrB_2 -SiC TPS are presented in Figure D.5 comparing them with the temperature profile obtained for the same material in literature (Savino *et al.*, 2005). The results show that discrepancies between the benchmark temperature-profile and the computed one are well within 5%.

D.3.4 Phenolic-Nylon ablative material

The convective and radiative heat fluxes used to validate the performance of the thermal model with the Phenolic-Nylon TPS are presented in Figure D.6. With an initial thickness of $18mm$, the performance of our model are compared to the results obtained in the original report (Delgado Montes, 1989). The

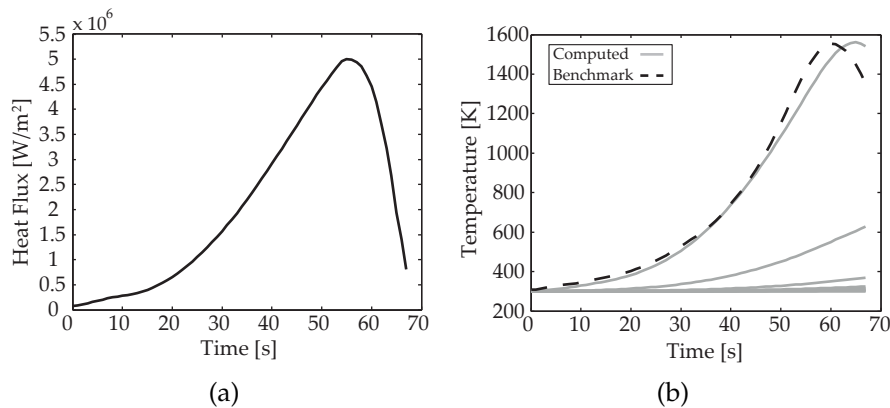


Figure D.5 UHTC ZrB₂-SiC TPS. a) Incoming heat flux and (b) temperature profiles.

temperature and material recession trends are almost a perfect match, with the only inconvenient of a mild underestimation of the material recession.

D.3.5 Carbon-Phenolic ablative material

The performance of the thermal model with the Carbon-Phenolic TPS are compared to experimental results obtained with ground-tests with experimental billets of approximately 3.81 cm thickness (Sutton, 1970). The comparison of the experimental temperature data and the computed temperature profile are shown in Figure D.7. The temperature data in the high-enthalpy test facility was obtained with an equivalent constant heat-flux of $1.44w/m^2$, using an atmosphere with an oxygen mass fraction equal to 0.23.

D.3.6 PICA ablative material

For validating the model of the PICA ablative TPS, data from the Stardust Re-entry Capsule (SRC) is used. The SRC entered Earth's atmosphere with an inertial velocity of approximately 12.6 km/s. In past planetary missions with high entry heat-loads such as Pioneer-Venus or Galileo, Carbon-phenolic has been used as TPS material. The results obtained with our one-dimensional, stagnation-point, analysis are compared to the results obtained with a much more complete analysis performed in preparation of the Stardust mission (Olynick *et al.*, 1997). In particular, the results presented in Figure D.8 used as benchmark in this study, were obtained by using a two-temperature, non-equilibrium, axisymmetric flow solver, GIANTS2 (Gauss-Seidel Implicit Aerothermodynamic Navier-Stokes Code), coupled with a radiation process model, NOVAR2 (Nonequilibrium Optimized Vectorizable Radiation process model), adapted to incorporate the ablation phenomena. The entry trajectory was then discretized with seven points and laminar flow solutions with coupled radiation were generated with and without ablation. GIANTS/NOVAR and FIAT (Fully Implicit Ablation and Thermal response code) were combined to perform the TPS sizing (Olynick *et al.*, 1997). As shown in Figure D.8 the computed altitude-velocity profile matches the actual altitude-velocity path used to obtain the results in the literature (Olynick *et al.*, 1997). However, the peak heat-flux that we are able to compute is equal to $1.1Mw/m^2$, that is lower than the peak heat-flux of $1.2Mw/m^2$ used to compute the benchmark temperature profiles of figure D.8.

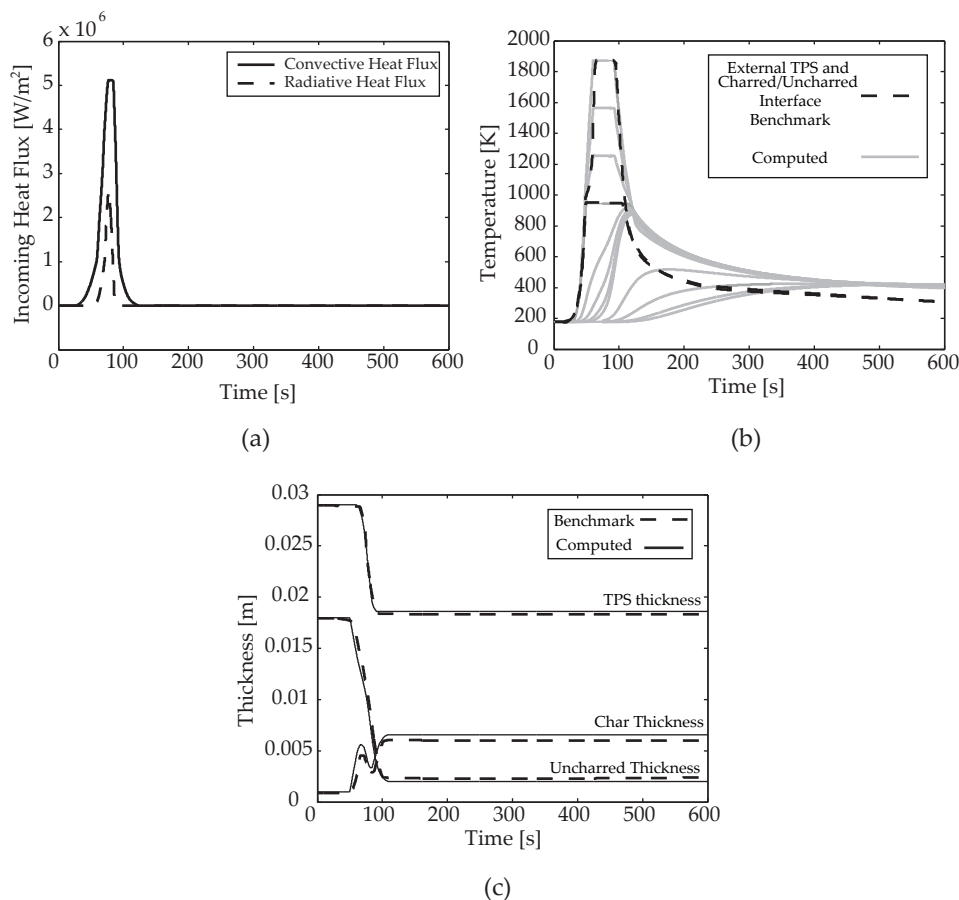


Figure D.6 Phenolic-Nylon TPS. (a)Benchmark re-entry capsule heat fluxes on the external surface, (b)comparison between benchmark and computed temperatures, and (c)material recession.

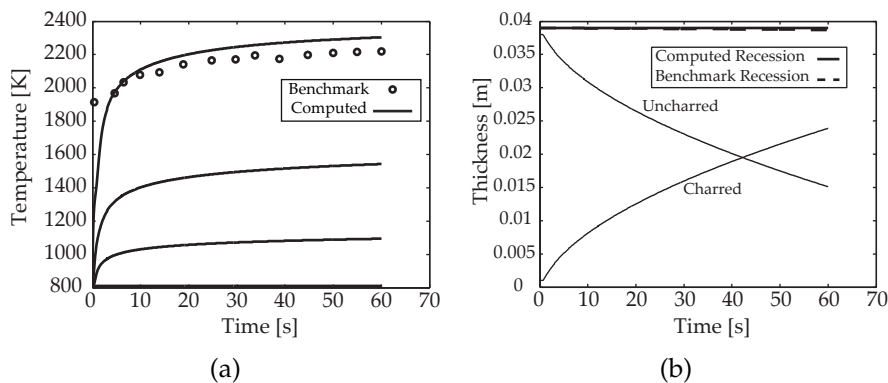


Figure D.7 Carbon-Phenolic TPS. Comparison between benchmark and computed (a) temperatures and (b) material recession.

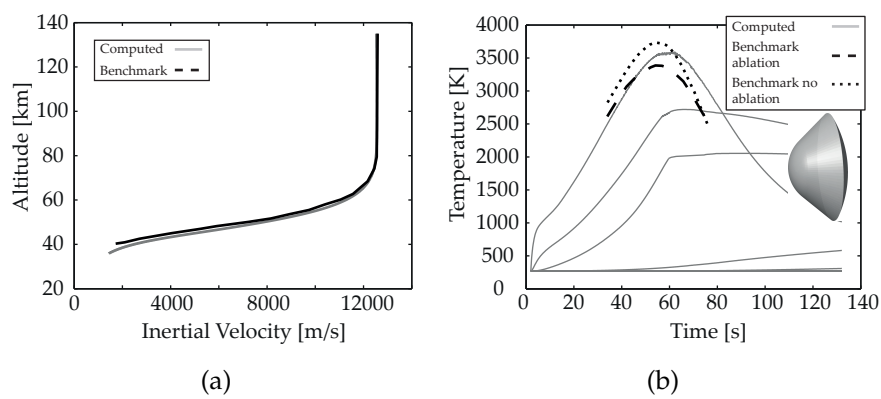


Figure D.8 PICA TPS. Comparison between benchmark and computed (a) altitude-velocity profile and (b) external layer temperature trends of the PICA TPS for the Stardust Re-entry Capsule.



Frustration of an aerospace engineer dealing with C++ memory allocation (Malloc) problems.

This is a humorous illustration presenting two entry capsules with slightly different shapes. One of them is very angry because it is behind the other one: it is losing the race. The other capsule, instead, has a very tedious problem to deal with: memory allocation. It is losing memory. The main purpose of this figure is to conclude this thesis with a funny figure drawn by the author during one of the most frustrating moments of his journey.

Memory allocation has nothing to do with an actual re-entry system. Re-entry capsules do not lose memory, eventually they (hopefully) only lose ablated material. In this case, memory allocation is something related to the computer code of the mathematical model developed for the analysis presented in this thesis. As said several times, building the mathematical models of the systems used as test cases was not the main purpose of the research. Nevertheless, mathematical models were necessary to demonstrate the methods proposed here. Building a proper mathematical model in the form of a computer code, using a robust programming language (e.g., C++), should actually be the subject of a separate PhD. As aerospace engineers, we are not the best candidates to build solid computer code, bugs free, with no memory allocation (or memory leaks) problems. We perform much better at a higher level, *i.e.*, setting the requirements for such programs and at a lower level, *i.e.*, using them. Memory leaks problems made me company for four long years. I could not help but acknowledge them. Thank you.

Curriculum Vitae

Guido Ridolfi was born in Salerno, Italy, on April 14, 1985. He attended secondary school at the scientific institute *Leonardo da Vinci*, in Vallo della Lucania. After obtaining his diploma, he started studying aerospace engineering at Politecnico di Torino. During his studies he won the *Erasmus* grant for attending his last year of the MSc at Delft University of Technology. He obtained his MSc degree from Politecnico di Torino in December 2008, with a thesis on the topic of engineering-tools development, for the design of satellite systems.

In January 2009 he started his PhD research in a cooperative framework between Delft University of Technology and Politecnico di Torino. The research described in this thesis culminated with a valuable experience in the ESA Concurrent Design Facility. During the course of his PhD he took part in other two important space-engineering activities. With Thales Alenia Space - Italy, he was principal investigator of a work package for the STEPS research program, funded by Piedmont region, Italy. He was also thermal engineer and manager of the thermal-tests campaign of the cubesat *e-st@r*, developed at Politecnico di Torino.